

Process Modeling of Ti-6Al-4V Linear Friction Welding (LFW)

Mica Grujicic, G. Arakere, B. Pandurangan, C.-F. Yen, and B.A. Cheeseman

(Submitted October 10, 2011)

A fully coupled thermomechanical finite-element analysis of the linear friction welding (LFW) process is combined with the basic physical metallurgy of Ti-6Al-4V to predict microstructure and mechanical properties within the LFW joints (as a function of the LFW process parameters). A close examination of the experimental results reported in the open literature revealed that the weld region consists of a thermo-mechanically affected zone (TMAZ) and a heat-affected zone (HAZ) and that the material mechanical properties are somewhat more inferior in the HAZ. Taking this observation into account, a model for microstructure-evolution during LFW was developed and parameterized for the Ti-6Al-4V material residing in the HAZ. Specifically, this model addresses the problem of temporal evolution of the prior β -phase grain size (the dominant microstructural parameter in the HAZ) during the LFW process. This model is next combined with the well-established property versus microstructure correlations in Ti-6Al-4V to predict the overall structural performance of the LFW joint. The results obtained are found to be in reasonably good agreement with their experimental counterparts suggesting that the present computational approach may be used to guide the selection of the LFW process parameters to optimize the structural performance of the LFW joints.

Keywords linear friction welding, process modeling, Ti-6Al-4V, weld microstructure/properties prediction

1. Introduction

Linear friction welding (LFW) is one of the solid-state frictional-sliding-based joining processes. A schematic of this process is depicted in Fig. 1. It is seen that the process involves (relative) reciprocating linear motion of the two workpieces to be joined (due to frictional heating of the workpiece material adjacent to the faying/contacting flat surfaces). This joining process is an adaptation/extension of the more common rotational friction welding process (used for welding workpieces with cylindrical geometry like pipes, rods, etc.) to non-cylindrical workpiece geometries.

Close examination of the LFW process reveals five distinct phases (Ref 1-3):

- (a) *Initial phase*: In this phase, the two workpieces are placed under contact pressure (along flat-conforming contact surfaces) and brought into a mutually reciprocating linear motion, in the presence of an inert gas. As the reciprocating motion under contact pressure continues further, the amount of wear-debris and the contact temperature

increase causing an increase in the inter-workpiece friction coefficient as well as an increase in the *true* contact surface area. This phase (in particular, achievement of a proper temperature) plays a critical role in attaining a good quality weld;

- (b) *Transition phase*: During this phase, the size of the wear particles increases, and the true contact surface area reaches its maximum value (i.e., becomes nearly equal to the nominal contact surface area). The temperature in the contact region also increases, causing the formation of a softened/plasticized contact region. Furthermore, due to its low strength and the presence of high contact pressures and shear stresses, this plasticized region undergoes plastic deformation. Concurrently, the thermo-mechanically affected zone (TMAZ) and the heat affected zone (HAZ) extend into the bulk of the workpiece from the contact-surface asperities;
- (c) *Equilibrium phase*: In this phase, a higher contact/upsetting pressure is applied to the faying surfaces of the workpieces. In combination with the oscillatory motion, this causes extrusion/expulsion of the highly plasticized material from the contact region, the formation of a flash and the reduction of the workpiece dimension in the direction normal to the weld (the so-called *axial shortening*). The presence of a single flash (as opposed to the presence of two diverging flashes) is typically an indication of a good quality weld (Ref 2);
- (d) *Deceleration/Forging phase*: Within this phase, the reciprocating linear motion is abruptly (in less than 0.1 s) stopped while still higher (forging) pressures are applied (for approx. 5-10 s) to consolidate the weld; and
- (e) *Stand phase*: At the beginning of this phase, the inert gas supply is cut-off, while the forging pressure is gradually reduced to zero as the weldment temperature reduces to

Mica Grujicic, G. Arakere, and B. Pandurangan, Department of Mechanical Engineering, Clemson University, 241 Engineering Innovation Building, Clemson, SC 29634-0921; and C.-F. Yen, and B.A. Cheeseman, Army Research Laboratory, Survivability Materials Branch, Aberdeen Proving Ground, MD 21005-5069. Contact e-mail: gmica@clemson.edu.

Report Documentation Page				Form Approved OMB No. 0704-0188	
Public reporting burden for the collection of information is estimated to average 1 hour per response, including the time for reviewing instructions, searching existing data sources, gathering and maintaining the data needed, and completing and reviewing the collection of information. Send comments regarding this burden estimate or any other aspect of this collection of information, including suggestions for reducing this burden, to Washington Headquarters Services, Directorate for Information Operations and Reports, 1215 Jefferson Davis Highway, Suite 1204, Arlington VA 22202-4302. Respondents should be aware that notwithstanding any other provision of law, no person shall be subject to a penalty for failing to comply with a collection of information if it does not display a currently valid OMB control number.					
1. REPORT DATE OCT 2012		2. REPORT TYPE		3. DATES COVERED 00-00-2012 to 00-00-2012	
4. TITLE AND SUBTITLE Process Modeling of Ti-6Al-4V Linear Friction Welding (LFW)				5a. CONTRACT NUMBER	
				5b. GRANT NUMBER	
				5c. PROGRAM ELEMENT NUMBER	
6. AUTHOR(S)				5d. PROJECT NUMBER	
				5e. TASK NUMBER	
				5f. WORK UNIT NUMBER	
7. PERFORMING ORGANIZATION NAME(S) AND ADDRESS(ES) Clemson University, Department of Mechanical Engineering, 241 Engineering Innovation Building, Clemson, SC, 29634				8. PERFORMING ORGANIZATION REPORT NUMBER	
9. SPONSORING/MONITORING AGENCY NAME(S) AND ADDRESS(ES)				10. SPONSOR/MONITOR'S ACRONYM(S)	
				11. SPONSOR/MONITOR'S REPORT NUMBER(S)	
12. DISTRIBUTION/AVAILABILITY STATEMENT Approved for public release; distribution unlimited					
13. SUPPLEMENTARY NOTES					
14. ABSTRACT					
15. SUBJECT TERMS					
16. SECURITY CLASSIFICATION OF:			17. LIMITATION OF ABSTRACT Same as Report (SAR)	18. NUMBER OF PAGES 13	19a. NAME OF RESPONSIBLE PERSON
a. REPORT unclassified	b. ABSTRACT unclassified	c. THIS PAGE unclassified			

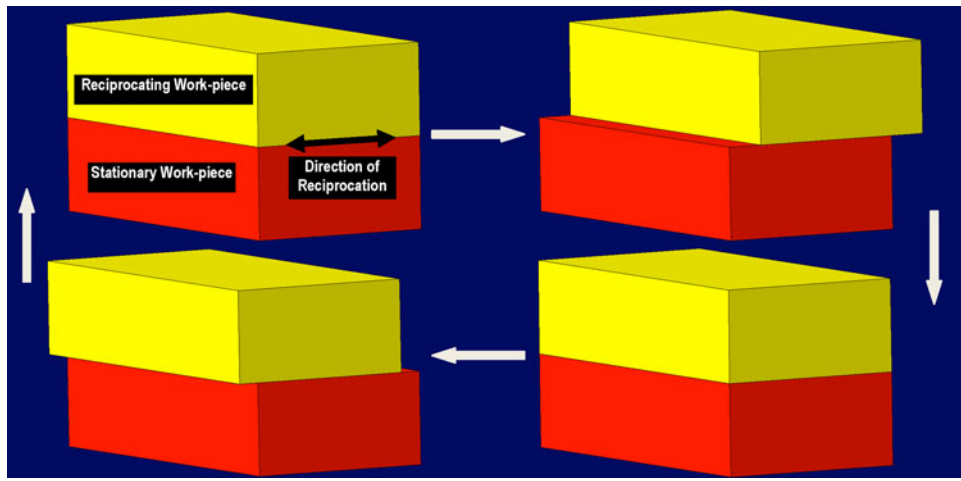


Fig. 1 A schematic of the Linear Friction Welding (LFW) process

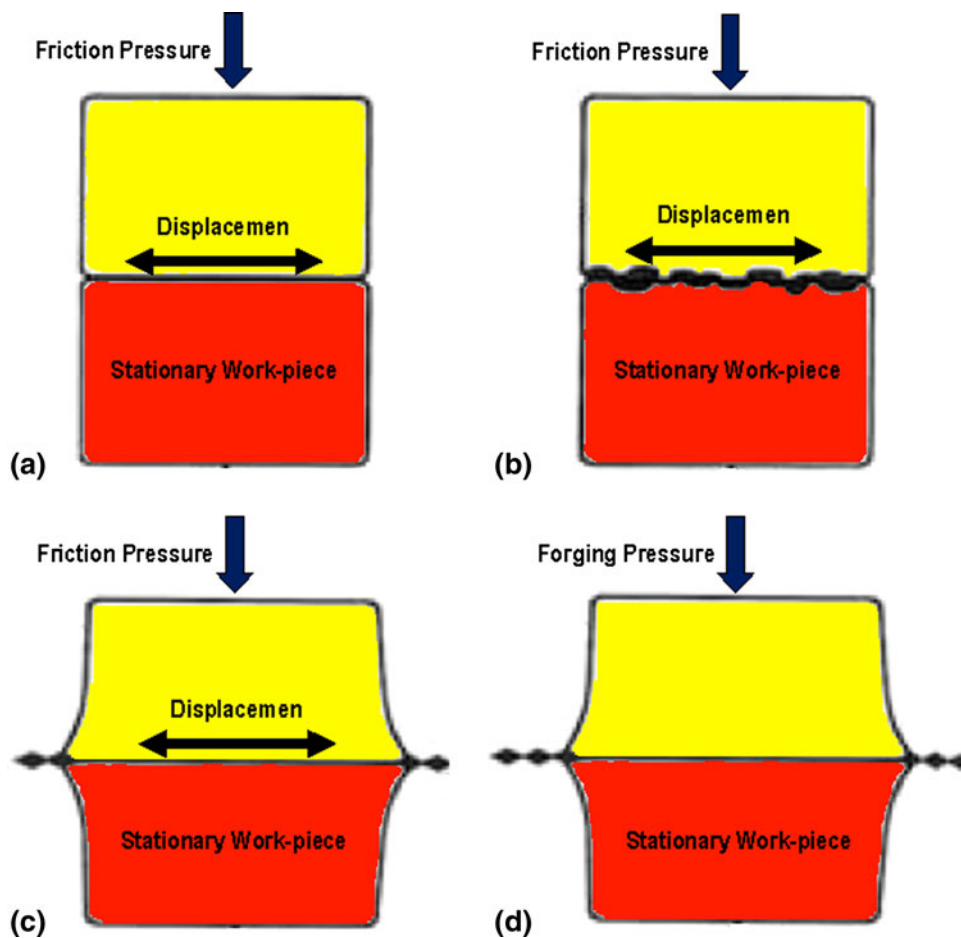


Fig. 2 First four phases of the LFW process: (a) Initial phase; (b) transition phase; (c) equilibrium phase; and (d) deceleration/forging phase

room temperature (Ref 4). The weld region experiences microstructural changes due to attendant recrystallization and creep as well as dimensional changes (primarily in a direction normal to the faying surfaces, axial shortening). A simple schematic of the first four phases of the LFW process is depicted in Fig. 2.

For a given choice of the workpiece materials to be joined, the main LFW process parameters are as follows: (a) frequency of reciprocating motion; (b) amplitude of reciprocating motion; (c) temporal variation of contact/upsetting/forging pressure; (d) total duration of LFW process; and (e) the geometry of the contacting surfaces. These parameters (or more precisely their

combination) may in general, have a major effect on the quality and structural integrity of the resulting weld.

Like other versions of the frictional welding process, LFW offers a number of advantages over the conventional fusion welding processes: (a) ability to join even in the absence of melting and re-solidification processes; (b) a narrow HAZ due to a highly pronounced localization of the heat generated at the faying surfaces; (c) suitability for joining difficult-to-weld, high-performance, and dissimilar (metallic) materials (e.g., joining of the aircraft-engine blades (made of alloy grades with superior high-temperature and high-cycle fatigue properties) to disks (made of alloy grades with superior low-cycle fatigue properties) (Ref 5); (d) good mechanical properties of the weld and low overall distortion of the weldment; (e) no need for the use of an external heat source; (f) utilization of relatively low reciprocating axial speeds; (g) improved safety due to the absence of toxic fumes or the spatter of molten material; (h) ease of process automation; (i) low environmental impact; and (j) can be used to weld non-metallic materials. However, some disadvantages of the LFW process have also been identified: (a) resulting in formation of flash (containing the workpiece material which was initially adjacent to the contacting surfaces, was heated-up and softened during the welding process, and ultimately squeezed out) removal of which requires costly post-weld machining; (b) only being applicable to joining workpieces with relatively high shear strength; (c) requiring relatively complex and precise control systems; and (d) requiring the use of large-capacity high-stiffness fixturing systems and high-capacity (typically hydraulic) presses.

While LFW is becoming more frequently used in automotive, spacecraft construction, tool manufacturing, pipeline construction, and other energy-related industries, because of the high-cost, it is currently employed mainly in the manufacture of aircraft engines (where the high value-added cost of the components justifies the cost associated with this process). For example, separate manufacture of aircraft-engine blades and disks and their subsequent joining using LFW is cost effective relative to the conventional production of the blade/disk (blisks) assemblies from single billets via machining.

Examination of the open-domain literature carried out as part of the present study revealed that LFW has been successfully used in joining of various metal-alloy grades, such as (a) titanium alloys (e.g., Ref 6-9); (b) superalloys (Ref 10); (c) steel (Ref 11, 12); and (d) intermetallics (Ref 13).

Detailed studies of the LFW process carried out over the last 10-20 years have clearly established that the temperature in the contact region plays a dominant role in the joining process affecting the phenomena, such as welding efficiency, spatial distribution, and temporal evolution of material deformation and microstructure fields as well as quality/structural integrity of the weld. Experimental measurements of the LFW temperature fields, however, are quite challenging and associated with considerable uncertainty. That is the reason that considerable efforts in the recent years has been invested toward developing computational methods and tools for predicting LFW temperature (as well as deformation and microstructure) fields.

Among these recent efforts which appear most noteworthy are (a) D'Alvise et al. (Ref 14) developed a two-dimensional fully coupled thermomechanical finite-element model of the LFW process and used an innovative adaptive contact and re-meshing algorithm to simulate flash formation. The model predictions were found to be in reasonably good agreement with their experimental counterparts; (b) Sorina-Müller et al.

(Ref 4) developed a three-dimensional fully coupled thermo-mechanical finite-element model for the LFW process and applied it to Ti6Al2Sn4Cr6Mo alloy weldments. The computed results related to the temporal evolution of the axial shortening and the spatial distribution of various microstructural phases/constituents and microhardness in the as-LFWed material state are found to be in very good agreement with the corresponding experimental data.

Cumulative experience with the LFW since invention of this joining process clearly established that the quality, microstructure, and properties of the welds are governed by the aforementioned LFW process parameters. Considering the importance of LFW in the production of air-craft engine blisks, there have been a number of attempts to establish the effect of various LFW process parameters on the material microstructure (Ref 9, 15), texture (Ref 10, 16), and weld properties (Ref 11, 17), as well as to identify the optimal combination of LFW process parameters (e.g., Ref 1-3). These efforts show that while, through extensive experimentation, the process/microstructure/property relations and the optimal sets of LFW process parameters can be established for a given combination of the workpiece material grades and temper, these findings cannot be easily extended to other combinations of the LFW workpiece materials. This is not surprising considering the complicated nature of interaction between the thermomechanical environment and the material microstructure within the highly non-uniform weld region. To overcome this shortcoming of the purely experimental efforts, an attempt is made in the present study to develop a preliminary LFW process model and apply it to a widely used Ti-6Al-4V titanium-alloy grade. To achieve this end, advanced coupled thermomechanical computational analyses involving adaptive meshing and material microstructure evolution are employed.

The organization of the article is as follows: The key physical-metallurgy aspects of Ti-6Al-4V are reviewed in section 2. The LFW behavior of the same alloy is discussed in section 3. The fully coupled thermomechanical finite-element analysis used in the LFW process modeling computational is overviewed in section 4. Main computational results obtained are presented and compared with their experimental counterparts in section 5. The main conclusions resulting from the present study are summarized in section 6.

2. Physical Metallurgy of Ti-6Al-4V

Before one can expect to successfully complete the task of understanding the effect of FSW process parameters on the material microstructure and properties in different zones of a Ti-6Al-4V weld, it is critical that a reasonably good understanding of the physical metallurgy of this alloy be acquired (e.g., Ref 18). Specifically, one should become familiar with all the stable and metastable phases present in this alloy system, thermal (and mechanical) conditions under which these phases are formed, the effect of the material thermal-mechanical history on its microstructure as well as the basic correlations between the phases present, their morphologies, and the resulting material properties. In the remainder of this section, a brief overview of these aspects of the Ti-6Al-4V physical metallurgy is provided.

Pure titanium undergoes, during heating, an allotropic phase transformation from a low-temperature hexagonal close-packed

α phase to the high-temperature body-centered cubic β phase at a (*beta transus*) temperature of 882.5 °C. Alloying elements can stabilize thermodynamically either the α - or the β -phase, i.e., increase or decrease the beta-transus temperature (range). Consequently, titanium alloys may contain at room temperature different relative amounts of the two phases and are typically classified as α -type, $\alpha + \beta$ -type, and β -type alloys. Among titanium alloys, $\alpha + \beta$ -type are of particular interest since vastly different mechanical properties can be imparted through the use of various thermomechanical treatments.

Ti-6Al-4V alloy analyzed in the present study falls into the category of $\alpha + \beta$ -type titanium alloys. This alloy is generally considered as the workhorse of the titanium industry and accounts for more than 50% of the total titanium consumption. The alloy offers a good overall combination of the properties, such as low density, high strength/stiffness, reasonably good corrosion resistance, good hot, warm, and cold formability, and superior weldability with respect to fusion-based welding techniques. The maximum service temperature for Ti-6Al-4V alloy is generally quoted as 350 °C.

To obtain different combinations of material properties in Ti-6Al-4V, the following heat treatments are most often employed.

Mill annealing: Consists of a high-temperature soaking treatment within the $\alpha + \beta$ or β -phase region followed by air cooling. The primary purpose of this (often incomplete) heat treatment is to remove heavily deformed microstructures resulting from cold/warm working.

Recrystallization annealing: Consists of a sufficiently long soaking treatment in the high-temperature portion of the $\alpha + \beta$ phase region followed by slow cooling.

Beta-annealing: Same as the recrystallization annealing except that the soaking is done in the single β -phase region. Both recrystallization and beta-annealing treatments improve material fracture toughness.

Stabilization annealing: Same as the recrystallization annealing except that the soaking is done in the lower-temperature portion of the $\alpha + \beta$ phase region. This results in an increased partitioning of the β -phase-stabilizing elements to the β -phase, reducing the probability for formation of an embrittling metastable ω -phase.

Stress-relief annealing: Same as the stabilization annealing except that soaking is carried out over a shorter time period which is sufficient to relieve generally undesirable residual stresses via dislocation recovery/polygonization processes without measurably affecting material strength/ductility.

Vacuum annealing: The main purpose of this heat treatment is to *de-gas* the alloy, i.e., to remove deleterious interstitial elements/contaminants, such as oxygen, hydrogen, and nitrogen.

Solution treatment plus aging: Involves high-temperature soaking in the β -phase (and sometimes in the $\alpha + \beta$ phase) region followed by water quenching to room temperature and aging at an intermediate temperature.

The heat treatments like the ones discussed above are used to alter the material microstructure and, in turn, the mechanical properties of the alloy. While, only two phases (α and β) are normally observed in this alloy, the aforementioned heat treatments can produce vastly different microstructures/properties. Despite this alloy having been used for over 30 years, a complete knowledge of the basic microstructure/property relations is still lacking. Nevertheless, some of these relations are well established and will be explained later. To aid this

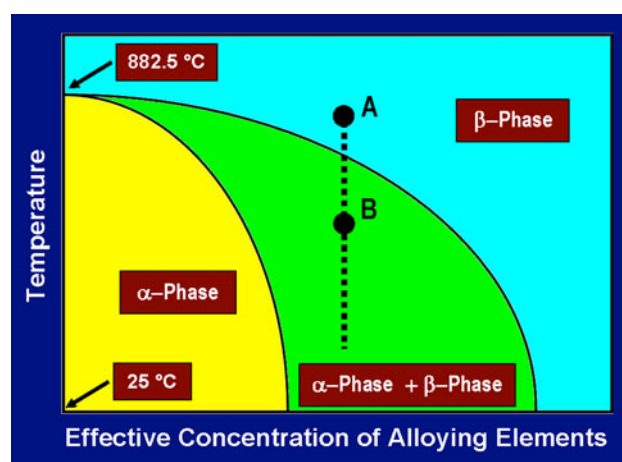


Fig. 3 A schematic of the Ti-based quasi-binary phase diagram in which the concentration of all alloying elements is lumped into a single quantity termed *Effective Concentration of Alloying Elements*. The nominal chemistry of the $\alpha + \beta$ Ti-6Al-4V alloy is indicated by the vertical dashed line

discussion, a schematic quasi-binary phase diagram is depicted in Fig. 3 in which the concentration of all alloying elements is represented by a single variable (an effective concentration) and defined along the x-axis.

When the alloy is soaked at a temperature exceeding the upper β -transus line (e.g., point A in Fig. 3), it transforms completely to the β -phase and if the soaking temperature is too high and/or if the soaking time is too long, it may suffer excessive grain growth (compromises quasi-static and dynamic strength). If the alloy is subsequently (air or furnace) cooled to room temperature (i.e., into the $\alpha + \beta$ region) a portion of the β -phase will transform into the α -phase (in the form of thin lamella grouped to form well-defined $\alpha + \beta$ lamellar colonies within the β -phase matrix/grains, Fig. 4a). This microstructural form of the α -phase is beneficial with respect to fracture toughness and stress corrosion cracking (SCC) resistance of the material.

When the alloy is quenched from the β -phase soaking temperature, the α -phase typically does not form, and instead the β -phase transforms martensitically (i.e., without any segregation/partitioning of the alloying elements) into an orthorhombic meta-stable α'' phase. During subsequent aging at an intermediate temperature, the orthorhombic phase re-transforms to a microstructure consisting of the β -phase matrix and fine, equiaxed α -phase precipitates (Fig. 4b). This type of microstructure is generally found to improve material's low and high cycle fatigue strengths as well as its fracture toughness.

When high-temperature soaking of the alloy is carried out within the $\alpha + \beta$ -phase region (e.g., point B in Fig. 3), the final microstructure contains the so-called primary α -phase particles. These particles are thermodynamically stable since they are formed as a result of material annealing in the two-phase region. The primary α -phase particles are generally globular in shape and since they form along the β -phase grain boundaries, they play a beneficial role in preventing excessive β -phase grain growth. During subsequent cooling to room temperature, additional α -phase is formed morphology of which depends on the cooling rate in the same way as that observed in the case of the alloy soaked in the β -phase region (Fig. 4c, d). It should be noted that depicted in Fig. 4(c) and (d) are smaller β -phase grains relative to those depicted in Fig. 4(a) and (b) to

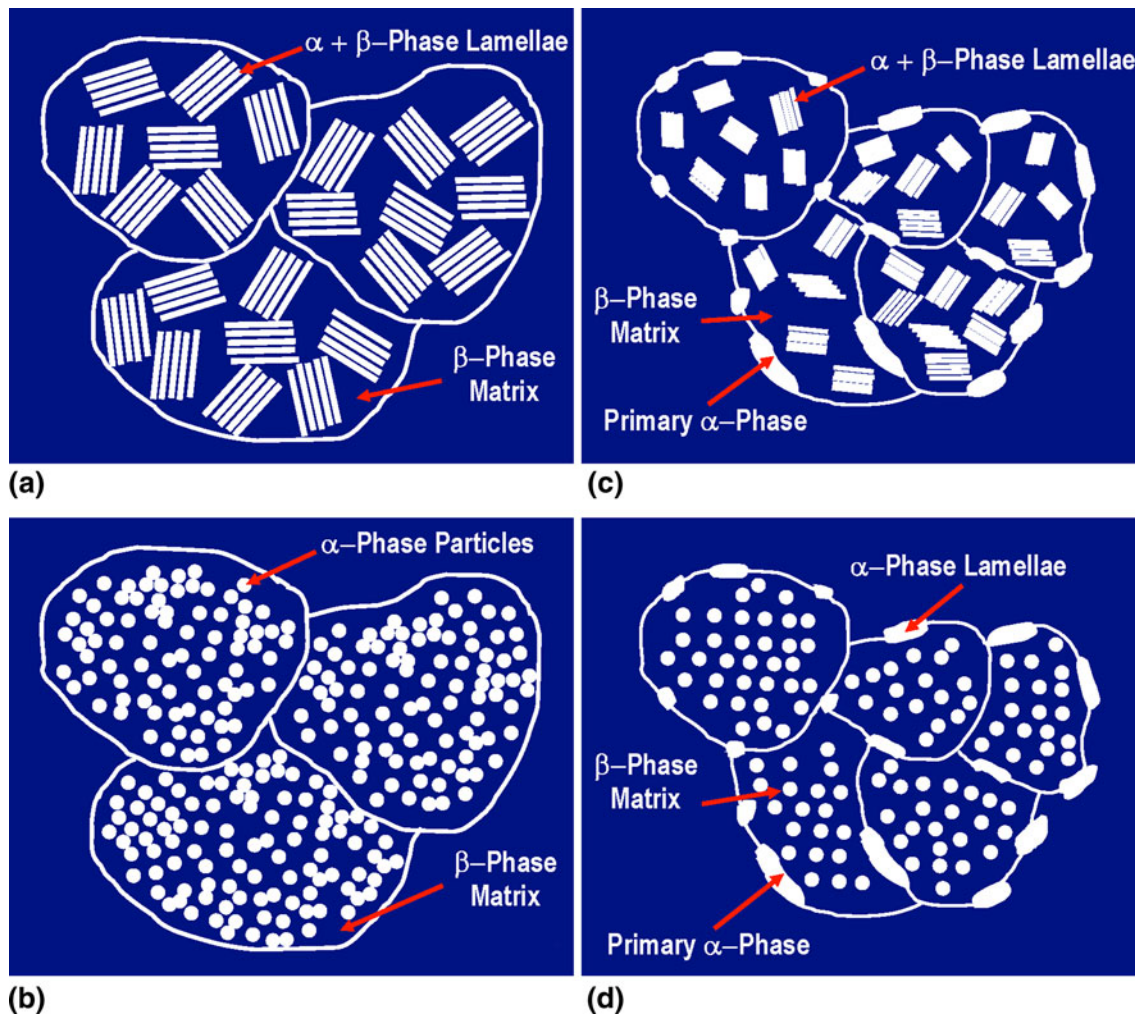


Fig. 4 A schematic representation of the Ti-6Al-4V material microstructures obtained after the following heat treatments: (a) β -phase soaking followed by slow cooling; (b) β -phase soaking followed by quenching and subsequent aging; (c) and (d) are, respectively, the same as (a) and (b) except that soaking is carried out in the $\alpha + \beta$ -phase region

graphically represent the beneficial role of primary α -phase particles in inhibiting β -phase grain growth. The presence of the primary α -phase particles and the resulting smaller-size β -phase grains and $\alpha + \beta$ colonies are typically found to improve material's fracture toughness and creep resistance. It should also be noted that soaking in the $\alpha + \beta$ -phase region results in the formation of a more stable β -phase (i.e., the β -phase with a higher amount of β stabilizing vanadium). This, in turn, can be beneficial since it reduces the tendency for formation of another metastable and highly embrittling ω -phase.

3. Linear Friction Welding Behavior of Ti-6Al-4V

While LFW of Ti-6Al-4V has been investigated experimentally by several researchers (e.g., Ref 1-3), the most comprehensive investigation of this type was reported by Vairis and Frost (Ref 1). In the remainder of this section, a brief description is provided of the basic behavior of Ti-6Al-4V during LFW as reported in Ref 1.

It should be noted that the Ti-6Al-4V used by Vairis and Frost (Ref 1) was in the mill-annealed condition (defined in

section 2). The reciprocation amplitude and frequency ranges used were 0.2-3.0 mm and 10-119 Hz, respectively. During the LFW process, the following quantities were monitored: (a) the axial position of the moving chuck (allows for the determination of the expelled material mass/volume); (b) the axial normal force; (c) tangential force (enables, along with the axial force, the determination of the interfacial friction coefficient) at the faying surfaces; and (d) weld peak temperature. Within the first four phases, the following main observations were made:

- (a) *Initial phase*: The tangential force was found throughout this phase to be fairly constant, displaying a balance between an increase in the contact surface area and a heat-induced decrease in the material strength. The weld peak temperature is of the order of 900 K;
- (b) *Transition phase*: Provided sufficient heat is generated in the initial phase, large wear particles begin to be expelled from the softened/plasticized interfacial region. This is accompanied by an increase in the tangential force, while no axial shortening takes place;
- (c) *Equilibrium phase*: As flash formation begins to take place in this phase, axial shortening begins and continues at a nearly constant rate. Weld peak temperatures

around ca. 1100 K are typically observed along with a nearly constant level of the tangential force. In this stage, Ti-6Al-4V shows relatively a high tendency toward thermal instability which results in non-uniform temperature distribution (and material expulsion) from different portions of the interface and may cause rotation of the contact interface (along with weld structural-integrity degradation); and

- (d) *Deceleration phase:* Good quality LFW joints in Ti-6Al-4V are achievable in this phase without additional contact pressure increase.

4. LFW Computational Analysis and Material Modeling

4.1 Computational Analysis

As mentioned earlier, modeling of the LFW process carried out in the present study employed a fully coupled thermomechanical finite-element procedure. This procedure is an extension of a similar procedure developed in our previous studies (Ref 18-26) for the friction stir welding process. In the remainder of this section, a detailed account of this procedure is provided.

4.1.1 Computational Domain. The computational domain used here consists of two (initially) parallelepiped-shaped workpieces with edge dimensions $L_x \times L_y \times L_z = 20 \text{ mm} \times 10 \text{ mm} \times 30 \text{ mm}$. The two workpieces are stacked in the z -direction so that the initial cross-sectional area of the two faying surfaces is $L_x \times L_y$ ($= 200 \text{ mm}^2$). In accordance with the common LFW process, reciprocating motion was assumed to take place along the shorter of the two contact-interface directions (y -direction, in the present case). This is done to facilitate flash formation (i.e., expulsion of the plasticized material) and to promote the formation of a good quality weld.

Each of the workpieces is meshed using first-order eight-node hexahedron (cubic or nearly cubic) thermomechanically coupled, reduced-integration finite elements. Owing to the transient nature of the temperature field and high-temperature sensitivity of the workpiece material properties, mesh-size (in the direction normal to the faying surfaces) is chosen in accordance with the steepest temperature gradient (and the stable time increment desired). Owing to the highly localized nature of the HAZ and TMAZ, a fine mesh had to be used only in the workpiece region near the contact interface. Typically each workpiece initially contained 18250 elements. An example of a typical finite element mesh used is depicted in Fig. 5 in which, for clarity, only the lower (stationary) workpiece is shown.

4.1.2 Computational Analysis Type. The LFW process is analyzed computationally using a fully coupled thermomechanical finite-element algorithm within which heat dissipation associated with tool/workpiece interfacial friction-sliding and plastic deformation is treated as a heat source in the governing thermal equation while the effect of temperature on the mechanical response of the workpiece material is taken into account through the use of a temperature-dependent workpiece material model.

4.1.3 Initial Conditions. The analysis is carried out by prescribing from the onset zero values to the stress and particle velocities and the ambient-temperature value to the temperature in both workpieces.

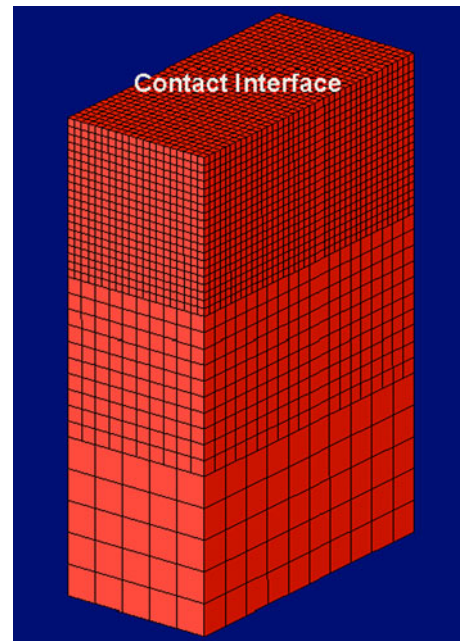


Fig. 5 Typical finite element mesh used in the present study. For clarity, only the lower workpiece is shown

4.1.4 Boundary Conditions. While LFW requires only the relative reciprocating motion of the contacting upper and lower workpieces, for convenience, the lower workpiece was kept stationary in the present study while the reciprocating motion is assigned to the upper workpiece. This was accomplished by assigning zero-displacement boundary conditions (in all three directions) to the bottom face of the lower workpiece. As far as the top face of the upper workpiece is concerned, it was constrained in the x -direction, subjected to a time-dependent pressure in the z -direction and assigned a sinusoidal/reciprocating displacement in the y -direction, u_y , as:

$$u_y = u_0 \sin(2\pi ft) \quad (\text{Eq 1})$$

where f is the frequency of reciprocating motion and u_0 is the amplitude.

As far as the thermal boundary conditions are concerned, it is assumed that the temperature at the outer surfaces of the workpieces is controlled by forced convection conditions (associated with the relative reciprocating motion of the workpieces). A typical value of $100 \text{ W/m}^2 \text{ K}$ was chosen for the convection coefficient. The same boundary condition was applied to the portions of the faying surfaces which were released (temporarily) from contact as a result of the reciprocating motion of the workpieces.

4.1.5 Contact Interactions. The workpiece-workpiece normal interactions are analyzed using a penalty-contact algorithm. Within this algorithm, penetration (normal) of the contacting surfaces is resisted by a set of linear springs, which produces a contact pressure that is proportional to the depth of penetration. Typically, maximum default values, which still ensure computational stability, are assigned to the (penalty) spring constants. Force equilibrium in a direction collinear with the contact-interface normal then causes the penetration to acquire an equilibrium (contact-pressure-dependent) value. It should be noted that no contact pressures are developed, unless (and until) the nodes on the *slave surface* contact/penetrate the

master surface. On the other hand, the magnitude of the contact pressure that can be developed is unlimited. As far as the tangential workpiece-workpiece interactions (responsible for transmission of the shear stresses across the contact interface) are concerned, they are modeled using a modified coulomb-friction law. Within this law, the maximum value of the shear stresses that can be transmitted (before the contacting surfaces begin to slide) is defined by a product of the contact pressure and a static (before sliding) and a kinetic (during sliding) friction coefficient. In addition, to account for the potential occurrence of a sticking condition (sliding occurs by shear fracture of the softer workpiece material, in the case of LFW of dissimilar materials, rather than by a relative motion at the contact interface), a maximum value of shear stress (equal to the shear strength of the softer material), which can be transmitted at any level of the contact pressure, is also specified. As far as the friction coefficient is concerned, it is generally recognized to be a function of a number of factors such as the (mean) interface temperature, contact pressure, slip speed, faying surface topology, etc. Following the study done in Ref 8, friction coefficient is assumed to be mainly affected by the interface temperature. Temperature dependence of the friction coefficient used in the present study is depicted in Fig. 6.

4.1.6 Heat Generation and Partitioning. As mentioned earlier, both frictional sliding and plastic deformation act as heat sources during the LFW process. The heat generated by these two phenomena in the workpiece contact region is subsequently partitioned between the two workpieces.

To account for the heat generated due to frictional sliding, it is assumed that its rate scales with the product of local interfacial shear stress and the sliding rate, and (in accordance with the standard practice; Ref 27) 90% of this energy is dissipated in the form of heat.

As far as work due to plastic deformation is concerned, 95% of this work was assumed to be dissipated in the form of heat because a small fraction of the plastic deformation work is stored in the form of crystal defects.

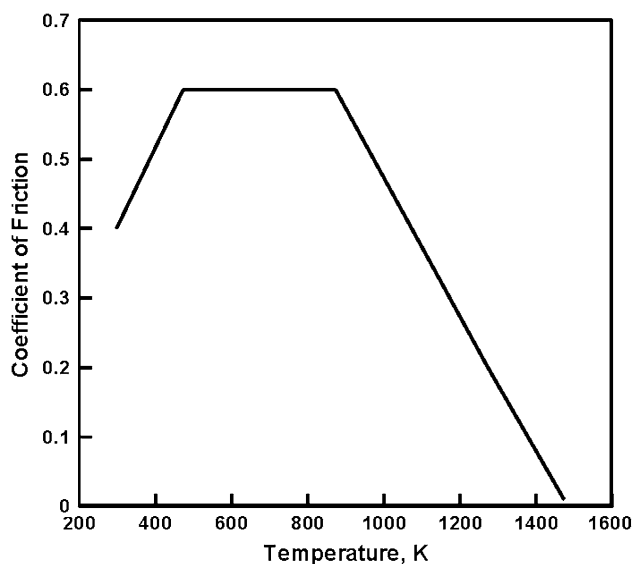


Fig. 6 Variation of friction coefficient with temperature during LFW of Ti-6Al-4V (Ref 12)

Partitioning of the heat generated during LFW between the two workpieces is computed using the procedure described in Ref 28. According to this procedure, the heat-ratio of the fraction of the heat allotted to the upper and lower workpieces is given by

$$\text{heat-ratio}_{\text{upper/lower}} = \frac{q_{\text{upper}}}{q_{\text{lower}}} = \sqrt{\frac{\lambda_{\text{upper}} \rho_{\text{upper}} c_{p_{\text{upper}}}}{\lambda_{\text{lower}} \rho_{\text{lower}} c_{p_{\text{lower}}}}} \quad (\text{Eq } 2)$$

where λ is thermal conductivity, ρ is the density, and c_p is the heat capacity of the workpiece material. The sum of the heat allotted to the two workpieces equals the total heat generated during frictional sliding. Examination of Eq 2 reveals that for identical materials of the two workpieces, as expected, the heat ratio is equal to unity.

In addition to the heat partitioning between the contacting workpieces, the problem of heat exchange/transfer between the same workpieces had to be addressed. In the present study, it was assumed that this heat exchange is of a purely conductive nature. While in the initial phase of LFW, the two workpieces contact only through surface asperities and air-filled gaps exist in the contact region, the roles of radiation and convection in the heat exchange between the workpieces were deemed negligible. This was done for the following reasons: (a) In the initial stage, the temperature in the contact region are too low for radiation to play any significant role; and (b) the interfacial-gap is small for the convective current to be formed. As far as the interfacial thermal conductance, h , is concerned, it is well established that it is a function of the surface topology, material thermomechanical properties, and contact pressure, P (Ref 29). The conductive heat transfer between the two contacting surfaces is defined as the product of the interfacial thermal conductance and the temperature difference between the two contacting surfaces.

4.1.7 Computational Algorithm. As established earlier, workpiece materials in the weld region experience large plastic deformations during LFW. Under these circumstances, the use of a pure Lagrangian approach in which the finite-element mesh is attached to and moves with the material may be prone to serious numerical problems (due to excessive mesh distortion). To overcome this potential problem, an Arbitrary Lagrangian Eulerian (ALE) formulation is used within which adaptive re-meshing of the highly distorted regions of the workpieces is carried out to maintain good quality mesh.

The fully coupled thermomechanical ALE problem associated with LFW process modeling is implemented in and solved using an explicit solution algorithm implemented in ABAQUS/Explicit (Ref 30), a general purpose finite element solver. As will be shown later, a material user-subroutine had to be developed and linked with this software to account for the workpiece material microstructural changes during LFW.

4.1.8 Computational Accuracy, Stability, and Cost. To keep the computational cost reasonable while ensuring accuracy and stability of the computational procedure, a mass scaling algorithm is used. This algorithm adaptively adjusts material density in the critical (time-step controlling) finite elements, without significantly affecting the computational analysis results.

4.2 Material Models

As mentioned earlier, LFW of Ti-6Al-4V is analyzed in the present study. In other words, both workpieces are made of the

Table 1 Johnson-Cook yield strength (σ_y) material model parameters(a) and the corresponding elastic and thermal parameters for Ti-6Al-4V

Parameter	Symbol	Units	Value
Reference strength	A	MPa	880.0
Strain-hardening parameter	B	MPa	695.0
Strain-hardening exponent	n	N/A	0.36
Strain-rate coefficient	C	N/A	0.04
Room temperature	T_{room}	K	293
Melting temperature	T_{melt}	K	1900.0
Temperature exponent	m	N/A	0.8
Young's modulus	E	GPa	113.8
Poisson's ratio	ν	N/A	0.34
Density	ρ	kg/m ³	4430
Thermal conductivity	k	W/m K	6
Specific heat	c_p	J/kg K	526

(a) $\sigma_y = [A + B(\bar{\epsilon}^{\text{pl}})^n] [1 + C \log(\dot{\epsilon}^{\text{pl}}/\dot{\epsilon}_0^{\text{pl}})] [1 - T_H^m]$

same material. Following our previous study (Ref 23), the workpiece material is assumed to be isotropic, linear-elastic and strain-hardenable, strain-rate sensitive, thermally softenable plastic material and is modeled using the Johnson-Cook material model (Ref 31). A summary of the Johnson-Cook material model parameters (including the yield stress, σ_y , governing equation) and the elastic and thermal properties of Ti-6Al-4V are provided in Table 1. In addition, temperature dependences of thermal conductivity and heat capacity of Ti-6Al-4V are depicted in Fig. 7(a) and (b), respectively (Ref 12).

It should be noted that in the original Johnson-Cook material model, temperature affects the material strength only reversibly by promoting thermal activation of dislocation motion. In other words, no permanent changes in the material microstructure and properties are assumed to result from a high-temperature exposure of the material. This assumption is not fully justified in the case of LFW where it is commonly observed that high temperatures in the weld give rise to the dynamic recovery/recrystallization with the accompanying sub-grain formation and grain size refinement. To account for this additional effect of temperature, a modification to the original Johnson-Cook model was proposed in our previous study (Ref 18). Essentially, strain hardening is still assumed to be related to the equivalent plastic strain: $\bar{\epsilon}_{\text{pl}}$, via a parabolic relation, $B\bar{\epsilon}_{\text{pl}}^n$, where B and n are material parameters (Table 1). However, $\bar{\epsilon}_{\text{pl}}$ is taken now to be composed of two terms: one (positive) associated with the operation of plastic deformation, and the other (negative) resulting from the operation of dynamic recrystallization. In other words, reduction in the dislocation density caused by dynamic recrystallization is modeled as an (apparent) effective reduction in the equivalent plastic strain, i.e., in the component of equivalent plastic strain which is responsible for strain hardening. On the other hand, the total equivalent plastic strain which measures the extent of irreversible overall deformation in the material is taken to remain unaffected by dynamic recrystallization.

While the original Johnson-Cook material model is available as a built-in model within ABAQUS/Explicit, the modifications of this model associated with the operation of dynamic recrystallization entail the development (and subsequent linking with the ABAQUS/Explicit solver) of a user-material subroutine (VUMAT). To validate the implementation of the material

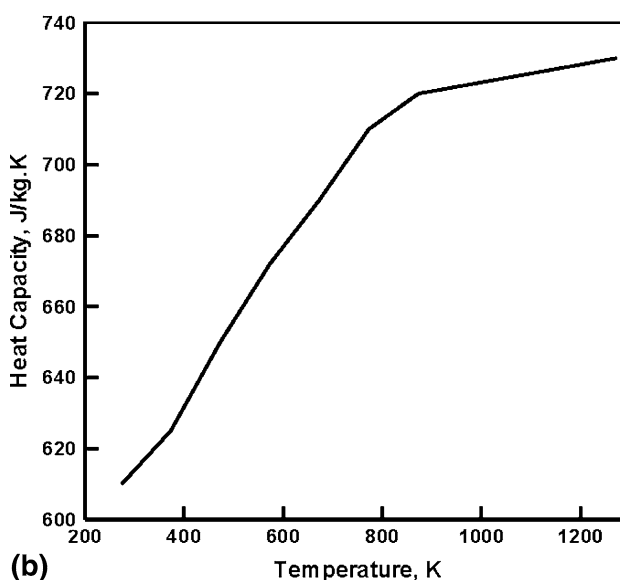
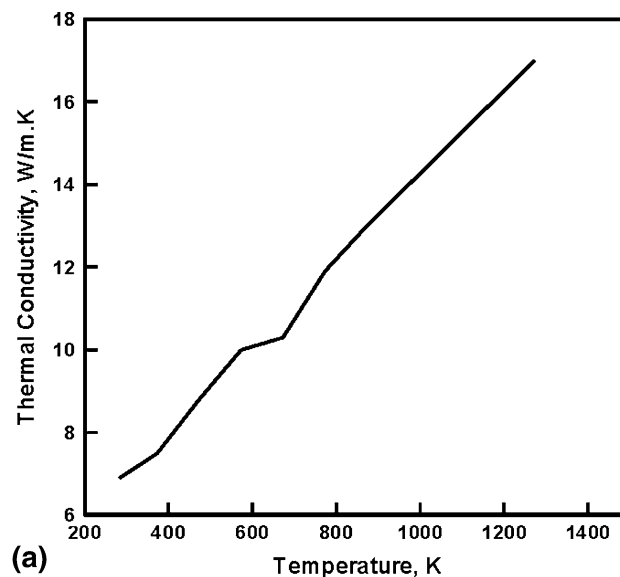


Fig. 7 Variation of (a) thermal conductivity and (b) heat capacity with temperature during LFW of Ti-6Al-4V (Ref 12)

model, several LFW cases were analyzed. It is found that when the effects of dynamic recrystallization are suppressed, the results (not shown for brevity), based on the user-material model and the built-in Johnson-Cook material model, are essentially identical.

4.3 Problem Definition

The main objective of the present study is to carry out a preliminary investigation of the LFW process parameters on the spatial distribution and temporal evolution of temperature and material flow in the weld region as well as the temporal evolution of axial shortening. The LFW process parameters considered include (a) reciprocation frequency; (b) reciprocation amplitude; and (c) contact pressure levels in different phases of LFW. A test matrix showing the levels of these parameters used in the present study is displayed in Table 2.

5. Results and Discussion

5.1 Typical Results

In this section, few typical results obtained in the present study are presented and discussed. These results deal with

Table 2 LFW process parameter test matrix used in the present study

Parameter	FSW phase			
	Initial	Transition	Equilibrium	Deceleration
Reciprocation amplitude, mm	0.5	1.5	2.5	N/A
Reciprocation frequency, Hz	20	30	40	N/A
Contact pressure, MPa	50	75	100	150

(a) spatial distribution and temporal evolution of the interface temperature; (b) temporal evolution and geometry of the expelled material/flash; and (c) temporal evolution of the axial shortening.

5.1.1 Spatial Distribution and Temporal Evolution of the Interface Temperature. From the standpoint of achieving a good quality weld, temperature uniformity over the contact interface, as well as the maximum value of the interface temperature are of major concern. This was the reason for monitoring, in the present study, these two aspects of the interface temperature during LFW.

An example of a typical temperature distribution over the contact interface is displayed in Fig. 8(a). The results displayed in this figure show that the temperature difference between the contact interface center and its edges is ca. 300 K. Depending on the choice of the LFW process parameters (reported in Table 2), this difference was found to range between 200 and 400 K. The main reason for the observed non-uniformity in the temperature distribution is the temporary loss of contact and the accompanying convective/radiation heat losses from the edge

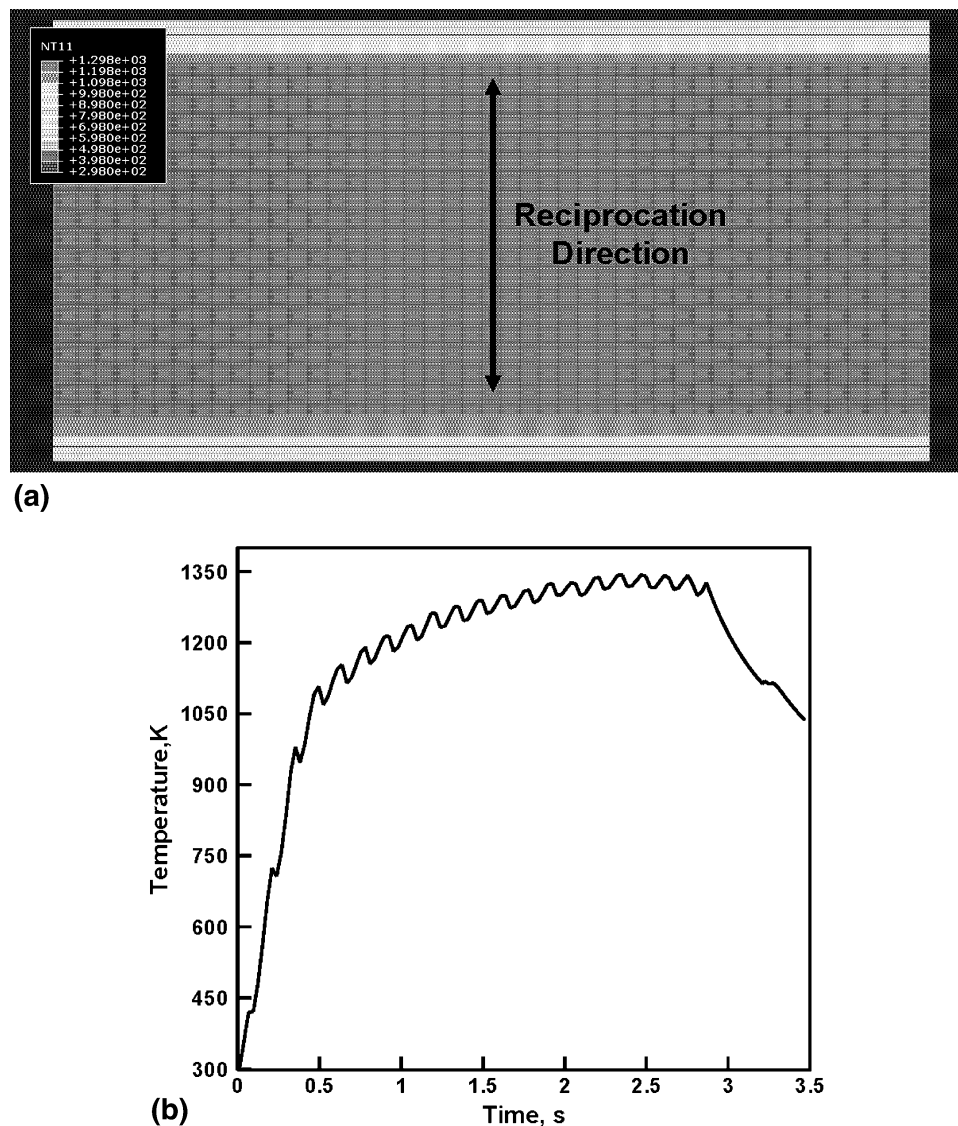


Fig. 8 Examples of the typical temperature-based results obtained in the present study: (a) spatial distribution of the temperature over the contact interface and (b) temporal evolution of temperature at the contact interface center point

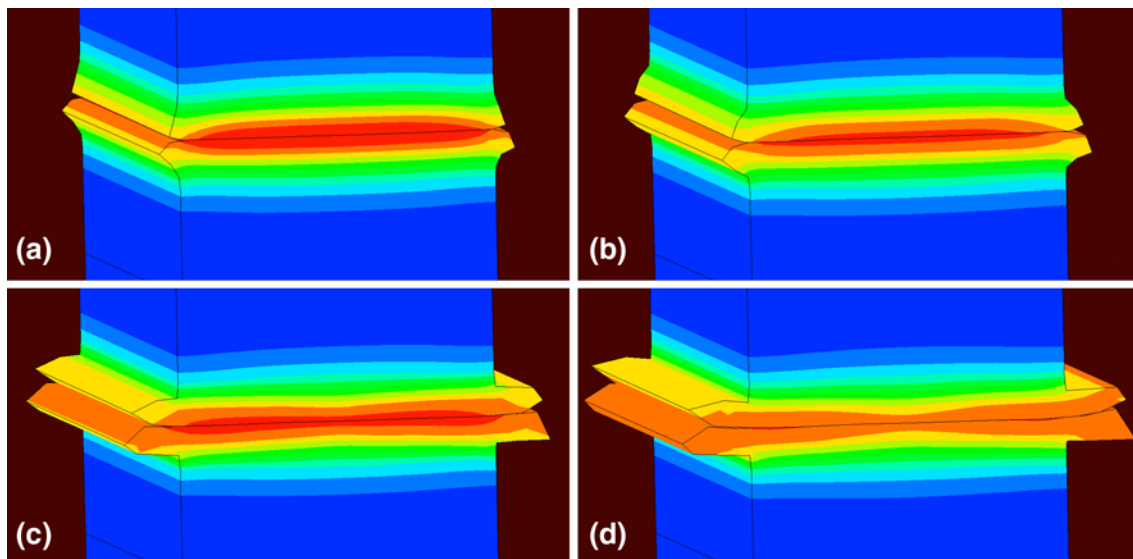


Fig. 9 Typical results pertaining to the temporal evolution of flash during LFW obtained in the present study. To help establish a relationship between the local temperature and the tendency/rate for flash formation, a (superimposed) surface temperature contour plot is also displayed

regions of the interface. Clearly, one of the objectives of the LFW process optimization is minimization of this temperature difference. The results obtained in the present study (not shown for brevity) clearly revealed that improved temperature uniformity was obtained at higher levels of the contact pressure.

An example of the temporal evolution of temperature at the contact-interface center point is shown in Fig. 8(b). It is seen that no melting takes place at this location (maximum temperature is lower than the melting temperature = 1900 K), while the $\alpha + \beta \rightarrow \beta$ -transus (= 1208 K) temperature has been exceeded. As will be discussed later, these findings have a major influence on the weld microstructure and properties.

5.1.2 Temporal Evolution and Geometry of the Expelled Material/flash. Typical results pertaining to the temporal evolution of flash during LFW are displayed in Fig. 9. For improved clarity, only a 30-mm-thick interfacial region is displayed in Fig. 9. Also, surface temperature contour plot is superimposed onto the material distribution plot in this figure to help relate the local temperature with the extent/rate of flash formation. Examination of the results displayed in Fig. 9 show that a single flash (on each workpiece side) is formed suggesting a good quality weld.

5.1.3 Temporal Evolution of the Axial Shortening. Typical results pertaining to the temporal evolution of axial shortening are displayed in Fig. 10. In general, depending on the choice of the LFW process parameters, the axial shortening start time ranges between 1 and 2 s. The results displayed in Fig. 10 are compared with their experimental counterparts (obtained under nominally identical specific LFW process conditions). This comparison revealed that the computed start time of axial shortening (ca. 2.5 s) is somewhat lower than its experimental counterpart (ca. 3 s). This disagreement can be attributed to the thermal radiation effects and the thermal conduction effects into the LFW-machine fixturing which were not accounted for in the present computational investigation.

5.2 Weld Microstructure and Properties

Previous experimental results (e.g., Ref 4), clearly established the presence of three distinct zones within LFW joints. A

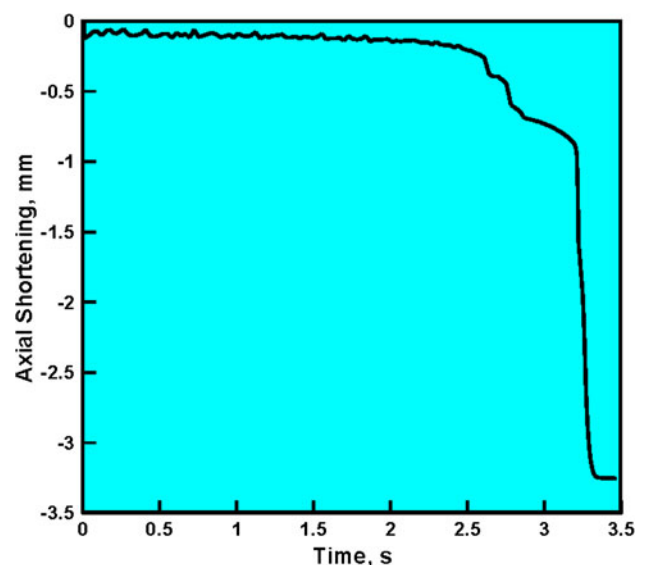


Fig. 10 Typical results pertaining to the temporal evolution of axial shortening obtained in the present study

brief description of the material microstructure and properties (primarily hardness) in these zones is provided shortly:

5.2.1 Weld-Center Zone. Ti-6Al-4V microstructure in this zone consists typically of very fine ($< 10 \mu\text{m}$) equiaxed grains indicating that severely deformed microstructure was dynamically recrystallized during LFW. Owing to a relatively short exposure of the material to high temperatures, it is believed that the occurrence of dynamic recrystallization implies exposure of the material in this region to temperatures exceeding the $\alpha + \beta \rightarrow \beta$ -transus temperature (since the rate of dynamic recrystallization is much higher in the single-phase beta region).

Experimental testing established that this portion of the weld is characterized by the superior mechanical properties (at least as judged by the hardness values). This finding is clearly related to the associated fine-grain microstructure and can be accounted

for using the traditional Hall-Petch relation. Typically, hardness values in a 450-500 HV range are found in this region.

5.2.2 Thermomechanically Affected Zone (TMAZ). This region contains heavily deformed material microstructure consisting of β -phase grains and α -phase particles elongated in the reciprocation direction (i.e., material-flow direction). Clearly, the temperature did not exceed the $\alpha + \beta \rightarrow \beta$ -transus temperature in this region.

Typical hardness values found in this region fall into the 360-400 HV range. These values are higher than those found in the base-metal revealing the effect of strain hardening.

5.2.3 Heat-Affected Zone (HAZ). In this region, no effect of plastic deformation on the material microstructure can be observed. However, owing to the exposure of the material to higher temperatures, microstructure coarsening is generally observed (relative to that found in the base metal region far away from the weld). The hardness values found in this region are the lowest, and they are even lower than those found in the base metal. This finding is the expected outcome of microstructure coarsening mentioned above.

5.3 Identification of the Most Critical Weld Zone

The discussion presented in the previous section clearly established that the HAZ is the weld region with the most inferior mechanical properties and is expected to control the overall mechanical performance of a LFW joints. Hence, understanding the microstructure evolution and microstructure-property relations in this region are of primary importance.

This region typically contains a bimodal room-temperature microstructure consisting of globular primary α -phase particles located along grain boundaries of the prior β -phase grains and $\alpha + \beta$ lamellar colonies. As mentioned earlier, this type of microstructure suggests that the material in the HAZ was never subjected to temperatures exceeding the upper β -transus line. The microstructure parameter which has the dominant effect on the strength and ductility of the material with this type of microstructure is the average size of the prior β -phase grains. A larger prior β -phase grain size (associated with prolonged material exposure to high temperatures approaching but remaining lower than the upper *beta-transus* line) generally compromises both the material strength and ductility making the HAZ the weakest section in the LFW joint.

Based on the discussion as above, the problem of relating the LFW process parameters to the structural performance of an LFW weldment reduces to the problem of establishment of correlations between the LFW process parameters and the HAZ-material microstructure/properties alone. Since, microstructure/property changes in the HAZ are only the result of the exposure of the material residing in this zone to high temperatures (i.e., plastic deformation has no effect in this region), the reduced problem, while still challenging, is considerably more tractable. That is, one needs to consider only the effect of temperature history of the material residing in this zone on its microstructure/properties. It should be noted that the temperature history of the material residing in the HAZ can be readily extracted from the results file generated during the aforementioned computational analysis of the LFW process. However, modeling of the material microstructure evolution (from the known initial microstructure) subjected to a given temperature history and the associated evolution in the material properties, two quite challenging problems, need to be addressed. The problems of microstructure and property evolution are handled in the next section.

5.4 Prediction of Microstructure/Property Evolution

Before dealing with the problem of modeling the evolution of material microstructure/properties within the HAZ during LFW, it should be recalled that the controlling microstructure parameter in this weld region is the prior β -phase grain size. In the present study, the correlations between the ultimate tensile strength/ductility and the prior β -phase grain size as reported in Ref 32 are used. These correlations are depicted graphically in Fig. 11. In addition, correlation between HAZ-material ultimate tensile strength, UTS, and, its Vicker's hardness, HV ($UTS \text{ (MPa)} = 3.27 \times HV \text{ (kgf/mm}^2\text{)}$) as reported in Ref 33 is also utilized in the present study. These correlations provide a unique opportunity to validate the present computational approach which relates the LFW process parameters with the resulting HAZ microstructure/properties. That is, if the present approach can predict the prior β -phase grain size for an arbitrary material point within the HAZ and for a given set of the LFW process parameters, then the corresponding ultimate tensile strength (and ductility) can be obtained from Fig. 11 and the associated Vicker's hardness be computed using the aforementioned correlation. Vicker's hardness computed in this way can then be compared with its readily obtainable experimental counterpart.

To complete the task described above, however, one must be able to model the evolution of the prior β -phase grain size over an arbitrary temperature history. In other words, one must be able to evaluate the following integral:

$$D = D_0 + \int_0^t \dot{D}(T(t), D(t), D_0) dt \quad (\text{Eq 3})$$

where D and D_0 are, respectively, the final and initial β -phase grain sizes, t is the time, T is the temperature, and a raised dot is used to denote a time derivative of a quantity.

To derive an expression for the grain-size growth rate, the isothermal grain-growth kinetics law reported in Ref 34 was used according to which

$$D(t, T) - D_0 = k(T)t^n \quad (\text{Eq 4})$$

where $k(T) (= k_0 e^{-\frac{Q}{RT}})$ is a temperature-dependent rate constant, $k_0 (= 9.88 \times 10^{-5} \text{ m/s}^n)$; $Q (= 56 \text{ kJ/mol})$ is the

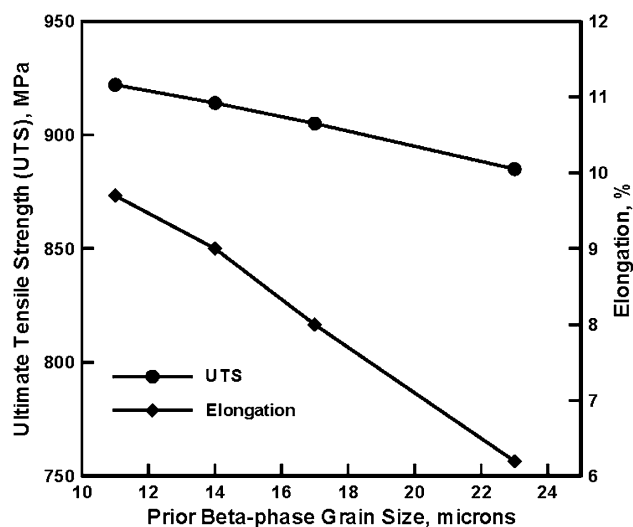


Fig. 11 Correlation between the primary β -phase grain size and the ultimate tensile strength in Ti-6Al-4V (Ref 32)

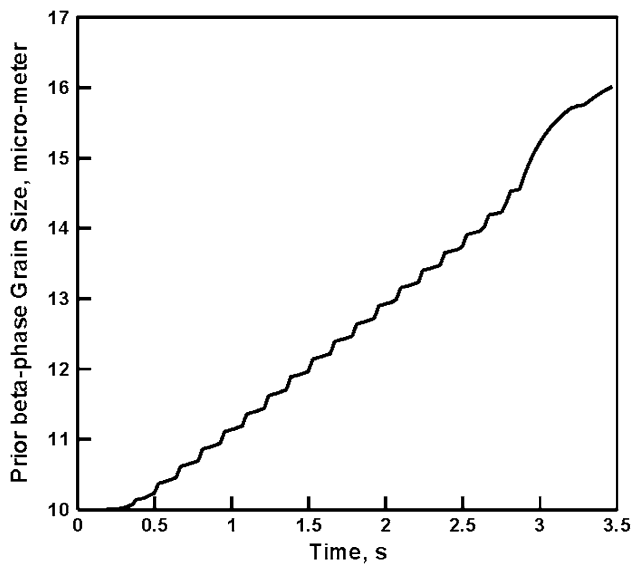


Fig. 12 A typical temporal evolution of the prior β -phase grain size within the HAZ

activation energy; R ($= 8.314$ J/mol K) is the universal gas constant; and n ($= 0.55$) a grain growth exponent. Using a simple mathematical procedure in which temperature is treated as a constant, and time is defined in terms of $D - D_0$, the integrated isothermal grain-growth law given by Eq 4, is converted into the corresponding (isothermal) grain growth rate equation in the form:

$$\dot{D}(T, D, D_0) = k(T)^{1/n} (D - D_0)^{(n-1)/n} \quad (\text{Eq 5})$$

Once Eq 5 is substituted into Eq 3, and T (appearing in the expression for k) is replaced by the temperature history $T(t)$, the final grain-size can be computed by numerically solving the resulting integral equation. Since the grain-size growth rate is a function of the current grain size, the integration has to be carried out sequentially starting with the first time increment. An explicit formulation was used in the present study in which D ($= D_{\text{beginning}}$) and T ($= T_{\text{beginning}}$) at the right-hand side of the modified Eq 3 are evaluated at the beginning of a time increment, and D ($= D_{\text{end}}$) evaluated as

$$D_{\text{end}} = D_{\text{beginning}} + \dot{D}(T_{\text{beginning}}, D_{\text{beginning}})(t_{\text{end}} - t_{\text{beginning}}) \quad (\text{Eq 6})$$

When the procedure described above is applied to the case of LFW process parameters reported in Ref 4, a HAZ-hardness value in the range 275–277 HV was obtained. This range is lower than the base metal hardness level (ca. 282.1 HV) and is in very good agreement with its experimental counterpart (ca. 273–278 HV) (Ref 4). The loss of hardness in the HAZ is the result of prior β -phase grain coarsening which is depicted in Fig. 12.

6. Summary and Conclusions

Based on the investigation and discussion as above, the following main summary remarks and related conclusions can be made:

- (1) A brief overview is provided of the key physical metallurgy and LFW behavior of Ti-6Al-4V, a commercially available Titanium alloy.
- (2) Based on the available results in the literature, it was concluded that the HAZ contains the most inferior properties and that it controls the overall structural performance of the weld.
- (3) A mathematical model is developed and parameterized for the temporal evolution of the prior β -phase grain size during the LFW process. This model is next combined with the well-established property versus microstructure correlations in Ti-6Al-4V to predict computationally mechanical properties within the HAZ.
- (4) The results obtained are found to be in reasonably good agreement with their experimental counterparts suggesting that the present computational approach may be used to guide the selection of the LFW process parameters to optimize the structural performance of the LFW joints (at least while they are controlled by the HAZ-material microstructure/properties).

Acknowledgments

The research material presented in this article is based on study supported by two Army Research Office sponsored grants (W911NF-11-1-0207 and W911NF-09-1-0513), and two U.S. Army/Clemson University Cooperative Agreements (W911NF-04-2-0024 and W911NF-06-2-0042).

References

1. A. Vairis and M. Frost, High Frequency Linear Friction Welding of a Titanium Alloy, *Wear*, 1998, **217**(1), p 117–131
2. A. Vairis and M. Frost, On the Extrusion Stage of Linear Friction Welding of Ti 6Al 4V, *J. Mater. Sci. Eng. A*, 1999, **271**(1), p 477–484
3. A. Vairis and M. Frost, Modeling the Linear Friction Welding of Titanium Blocks, *J. Mater. Sci. Eng. A*, 2000, **292**(1), p 8–17
4. J. Sorina-Müller, M. Rettenmayr, D. Schneefeld, O. Roder, and W. Fried, FEM Simulation of the Linear Friction Welding of Titanium Alloys, *Comput. Mater. Sci.*, 2010, **48**, p 749–758
5. M. Corzo, Y. Torres, M. Anglada, and A. Mateo, Fracture Behaviour of Linear Friction Welds in Titanium Alloys, *Anales de la Mecánica de Fractura*, 2007, **1**, p 75–80
6. O. Roder, J.-P. Ferte, E. Gach, J. Mendez, M. Anglada, and A. Mateo, Development and Validation of a Dual Titanium Alloy Dual Microstructure BLISK, *Fifth Aeronautic Days 2006*, June 2006 (Vienna, Austria), 2006
7. P. Wanjara and M. Jahazi, Linear Friction Welding of Ti-6Al-4V: Processing, Microstructure, and Mechanical-Property Inter-Relationships, *Metall. Mater. Trans. A*, 2005, **36**(8), p 2149–2164
8. W.Y. Li, T.J. Ma, Y. Zhang, Q.Z. Xu, J.L. Li, S.Q. Yang, and H.L. Liao, Microstructure Characterization and Mechanical Properties of Linear Friction Welded Ti-6Al-4V Alloy, *Adv. Eng. Mater.*, 2008, **10**(2), p 89–92
9. M. Karadge, M. Preuss, C. Lovell, P.J. Withers, and S. Bray, Texture Development in Ti-6Al-4V Linear Friction Welds, *J. Mater. Sci. Eng. A*, 2007, **459**(2), p 182–191
10. M. Karadge, M. Preuss, P.J. Withers, and S. Bray, Importance of Crystal Orientation in Linear Friction Joining of Single Crystal to Polycrystalline Nickel-Based Superalloys, *J. Mater. Sci. Eng. A*, 2008, **491**(1), p 446–453
11. W.Y. Li, T.J. Ma, Q.Z. Xu, S.Q. Yang, Y. Zhang, J.L. Li, and H.L. Liao, Effect of Friction Time on Flash Shape and Axial Shortening of Linear Friction Welded 45 Steel, *Mater. Lett.*, 2008, **62**(2), p 293–296
12. T.J. Ma, W.Y. Li, Q.Z. Xu, Y. Zhang, J.L. Li, S.Q. Yang, and H.L. Liao, Microstructure Evolution and Mechanical Properties of Linear Friction Welded 45 Steel Joint, *Adv. Eng. Mater.*, 2007, **9**(8), p 703–707

13. P. Threadgill, *Linear Friction Welding, TWI, Knowledge Summary*, The Welding Institute, Cambridge, 2008
14. L. D'Alvise, E. Massoni, and S.J. Walløe, Finite Element Modeling of the Inertia Friction Welding Process Between Dissimilar Materials, *J. Mater. Process. Technol.*, 2002, **125–126**(9), p 387–391
15. M.R. Daymond and N.W. Bonner, Measurement of Strain in a Titanium Linear Friction Weld by Neutron Diffraction, *Phys. B*, 2003, **325**, p 130–137
16. P. Threadgill, Solid State Joining of Titanium Alloys, *Titanium World*, 1996, p 65–67
17. C. Mary and M. Jahazi, Linear Friction Welding of IN-718 Process Optimization and Microstructure Evolution, *Adv. Mater. Res.*, 2007, **15–17**, p 357–362
18. M. Grujicic, G. Arakere, B. Pandurangan, A. Hariharan, B.A. Cheeseman, C.-F. Yen, and C. Fountzoulas, Computational Analysis and Experimental Validation of the Friction-Stir Welding Behaviour of Ti-6Al-4V, *J. Eng. Manuf.*, 2011, **225**(2), p 208–223
19. M. Grujicic, T. He, G. Arakere, H.V. Yalavarthy, C.-F. Yen, and B.A. Cheeseman, Fully-Coupled Thermo-Mechanical Finite-Element Investigation of Material Evolution During Friction-Stir Welding of AA5083, *J. Eng. Manuf.*, 2010, **224**(4), p 609–625
20. M. Grujicic, G. Arakere, H.V. Yalavarthy, T. He, C.-F. Yen, and B.A. Cheeseman, Modeling of AA5083 Material-Microstructure Evolution During Butt Friction-Stir Welding, *J. Mater. Eng. Perform.*, 2010, **19**(5), p 672–684
21. M. Grujicic, G. Arakere, C.-F. Yen, and B.A. Cheeseman, Computational Investigation of Hardness Evolution during Friction-Stir Welding of AA5083 and AA2139 Aluminum Alloys, *J. Mater. Eng. Perform.*, 2010, doi:10.1007/s11665-010-9741-y
22. M. Grujicic, G. Arakere, B. Pandurangan, A. Hariharan, C.-F. Yen, and B.A. Cheeseman, Development of a Robust and Cost-Effective Friction Stir Welding Process for Use in Advanced Military Vehicle Structures, *J. Mater. Eng. Perform.*, 2011, **20**(1), p 11–23
23. M. Grujicic, G. Arakere, B. Pandurangan, A. Hariharan, C.-F. Yen, B.A. Cheeseman, and C. Fountzoulas, Computational Analysis and Experimental Validation of the Ti-6Al-4V Friction Stir Welding Behavior, *J. Eng. Manuf.*, 2010, **224**(8), p 1–16
24. M. Grujicic, G. Arakere, B. Pandurangan, A. Hariharan, C.-F. Yen, B.A. Cheeseman, and C. Fountzoulas, Statistical Analysis of High-Cycle Fatigue Behavior of Friction Stir Welded AA5083–H321, *J. Mater. Eng. Perform.*, 2010, doi:10.1007/s11665-010-9725-y
25. M. Grujicic, G. Arakere, A. Hariharan, and B. Pandurangan, A Concurrent Product-development Approach for Friction-stir Welded Vehicle-underbody Structures, *J. Eng. Manuf.*, 2010, doi:10.1007/s11665-011-9955-7
26. M. Grujicic, G. Arakere, B. Pandurangan, J.M. Ochterbeck, C.-F. Yen, B.A. Cheeseman, A.P. Reynolds, and M.A. Sutton, Computational Analysis of Material Flow During Friction Stir Welding of AA5059 Aluminum Alloys, *J. Mater. Eng. Perform.*, 2011, doi:10.1007/s11665-011-0069-z
27. P. Kes, *Beitrag zum Reibschweißen duktiler Eisengusswerkstoffe*, DVS-Verlag, Dusseldorf, 1989
28. S.J. Na, J. Ruge, and K. Thomas, Temperature Determination During the Friction Welding of Dissimilar Materials in Cylindrical Form-Measurement and Calculation. *Schweiss. Schneid.*, 1984, **36**(3), p E43–E45
29. M. Grujicic, C.L. Zhao, and E.C. Dusel, The Effect of Thermal Contact Resistance on Heat Management in the Electronic Packaging, *Appl. Surf. Sci.*, 2005, **246**, p 290–302
30. ABAQUS Version 6.10-EF1, *User Documentation*, Dassault Systems, 2010
31. G.R. Johnson and W.H. Cook, A Constitutive Model and Data for Metals Subjected to Large Strains, High Strain Rates and High Temperatures, *Proceedings of the 7th International Symposium on Ballistics*, 1983
32. Y. Zhang, Y.S. Sato, H. Kokawa, S.H.C. Park, and S. Hirano, Microstructural Characteristics and Mechanical Properties of Ti-6Al-4V Friction Stir Welds, *Mater. Sci. Eng. A*, 2008, **485**, p 448–455
33. M. Gupta and T.S. Srivatsan, Interrelationship Between Matrix Microhardness and Ultimate Tensile Strength of Discontinuous Particle-Reinforced Aluminum-Alloy Composites, *Mater. Lett.*, 2001, **51**, p 255–261
34. F.J. Gil and J.A. Planell, Grain Growth Kinetics of Near Alpha Titanium Alloys, *Mater. Sci. Lett.*, 2000, **19**, p 2023–2024